

Dzyaloshinskii-Moriya interaction induced magnetoelectric coupling in a tetrahedral molecular spin-frustrated system

Jie-Xiang Yu ¹, Jia Chen,¹ Neil Sullivan ², and Hai-Ping Cheng ^{1,*}

¹*Department of Physics, Center for Molecular Magnetic Quantum Materials and Quantum Theory Project, University of Florida, Gainesville, Florida 32611, USA*

²*Department of Physics and Center for Molecular Magnetic Quantum Materials, University of Florida, Gainesville, Florida 32611, USA*



(Received 14 October 2021; revised 5 June 2022; accepted 21 July 2022; published 9 August 2022)

We have investigated magnetoelectric (ME) coupling in the single-molecule magnet $\text{Mn}_4\text{Te}_4(\text{PEt}_3)_4$ with tetrahedral spin frustration. Our density functional studies found that an electric dipole moment can emerge with various noncollinear spin orderings. The forms of spin-dependent dipole are determined and consistent with that in noncentrosymmetric magnets driven by the Dzyaloshinskii-Moriya interaction. Writing a parameterized spin Hamiltonian, after solving for eigenvalues and eigenstates, we quantified the ME coupling by calculating the thermal average of the electric and magnetic susceptibilities, which can be influenced by external magnetic and electric fields, respectively. The quadratic relations are expected to be observable in experiments.

DOI: [10.1103/PhysRevB.106.054412](https://doi.org/10.1103/PhysRevB.106.054412)

I. INTRODUCTION

Considerable interest has been focused recently in the literature [1–6] on the search for multifunctional materials that couple magnetic and electric states through magnetoelectric (ME) interactions. Interest is not only for the fundamental science but also for the possible generation of electric-field-driven devices and their inherent low power dissipation compared with magnetically driven state changes found in conventional memory and related storage systems. In the search for ME materials, it is important to note that ME effects accompany both time-reversal and spatial inversion symmetry breaking. For example, the lattice-mediated ME effect usually happens when controllable ferroelectric properties without centrosymmetry coexist with a structure-sensitive spin state or spin ordering when time-reversal symmetry is broken. The distortion of the lattice influences both electric polarization and magnetization. In addition to conventional crystalline solids, such ME effects based on ionic displacement have been confirmed in molecule-based magnetic materials with lower Young's modulus [7–11].

Another origin of ME effect is the noncollinear magnetism characterized by the Dzyaloshinskii-Moriya (DM) interaction [12,13] in noncentrosymmetric magnets. In this theory, the polarization is described by $\hat{\mathbf{e}}_{ij} \times (\mathbf{S}_i \times \mathbf{S}_j)$, where $\mathbf{j}_{ij} = \mathbf{S}_i \times \mathbf{S}_j$ is the so-called spin supercurrent for two spins \mathbf{S}_i and \mathbf{S}_j , and $\hat{\mathbf{e}}_{ij}$ is the unit vector connecting the two spins [1,14,15]. The mechanism of the DM-induced ME effect is confirmed in some spiral magnetic systems such as rare-earth manganese TbMnO_3 and DyMnO_3 [16]. Although experiments found nonstructural induced ME effects in some polynuclear molecular nanomagnets [17,18], DM-induced ME effect studies in molecular magnets remain largely underinvestigated. Special

quantum features of the quantum spin states in molecular magnets that differentiate these systems from other crystalline materials can provide ME couplings with potential applications in quantum information science.

When we consider the symmetry of a molecular magnet, tetrahedral symmetry with point group T (chiral tetrahedral symmetry) is a rare example in which the absence of spatial inversion symmetry alone does not bring about a net polarization. Furthermore, an antiferromagnetic exchange interaction in a tetrahedral geometry can lead to frustrated spins, where the ground spin state can be uncertain and easily be altered by external fields. A representative multiferric crystal system with tetrahedral structure is Cu_2OSeO_3 which hosts magnetically induced polarization in the ferrimagnetic, helimagnetic, and skyrmion crystal phases [19–23] because of DM interaction. In contrast to the distorted Cu_4 tetrahedron that does not respect tetrahedral spin frustration, the $\text{Mn}_4\text{Te}_4(\text{PEt}_3)_4$ molecule where the magnetic center Mn_4 forms an equilateral tetrahedron in this paper is a magnetically frustrated unit. The crystalline phase of $\text{Mn}_4\text{Te}_4(\text{PEt}_3)_4$ shown in Fig. 1 has a body-centered-cubic lattice, and the space group is $I23(197)$ with point group T , so that both the global symmetry and local chemical environment respect a perfect tetrahedral symmetry.

In this paper, we have investigated both the magnetic properties and the electric polarization for various spin states of $\text{Mn}_4\text{Te}_4(\text{PEt}_3)_4$ based on density functional calculations. We confirmed the DM-induced ME effect in the molecular magnets. After solving the eigenvalues and eigenstates of the parameterized spin Hamiltonian, we quantified the ME coupling by calculating the thermal average of the electric susceptibility, which can be influenced by external magnetic field. The rest of the paper is organized as follows: In Sec. II, we describe the computational details; in Sec. III, we present results from density functional theory (DFT) calculation and the model Hamiltonian; and finally, in Sec. IV, we conclude our investigation.

*hping@ufl.edu

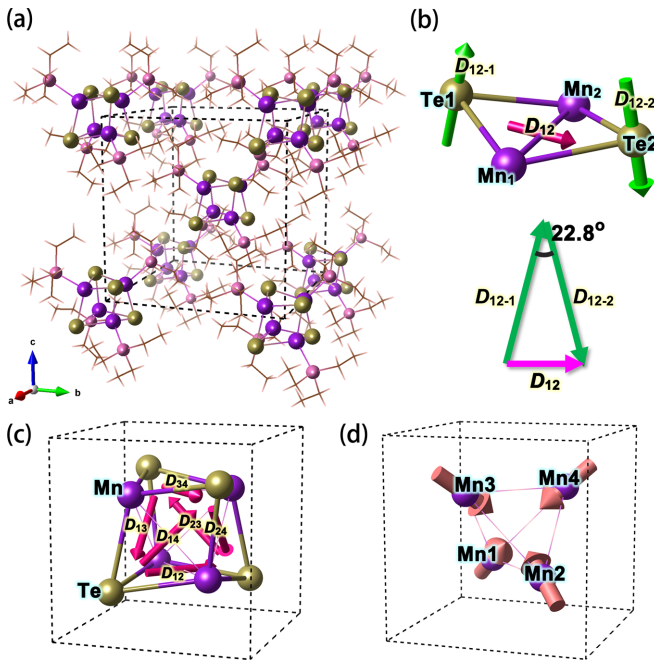


FIG. 1. (a) The crystalline phase of $\text{Mn}_4\text{Te}_4(\text{PEt}_3)_4$. Purple: Mn, dark yellow: Te, pink: P. (b) The Dzyaloshinskii-Moriya (DM) vector D_{12} of Mn1 and Mn2 composed of two DM vectors D_{12-1} and D_{12-2} perpendicular to two Mn-Te-Mn exchange paths, respectively. The apex angle in the isosceles triangle composed of D_{12-1} , D_{12-2} , and D_{12} is also shown. (c) The DM vectors between each two Mn and Te. (d) the axes of magnetic anisotropy of each Mn in $\text{Mn}_4\text{Te}_4(\text{PEt}_3)_4$.

II. COMPUTATIONAL METHODS

Our DFT-based calculations are performed with projector augmented wave pseudopotentials [24,25] implemented in the Vienna *Ab initio* Simulation Package (VASP) [26,27]. The generalized gradient approximation in the Perdew, Burke, and Ernzerhof (PBE) form [28] is used as the exchange-correlation energy, and the Hubbard U method ($U = 4.0$ eV, $J = 0.9$ eV) with density only and a spin-independent double counting scheme [29] is applied on Mn(3d) orbitals to include strong-correlation effects. An energy cutoff of 600 eV is used for the plane-wave expansion throughout the calculations. The DFT-D3 method [30] with inclusion of van der Waals correction is employed. For noncollinear spin orderings, spin-orbit couplings (SOCs) are included. The polarization vectors were obtained by the evaluation of the Berry phase expressions [31,32].

We use a body-centered cubic lattice with experimental lattice constant 13.174 \AA [33] including one $\text{Mn}_4\text{Te}_4(\text{PEt}_3)_4$ molecule for all calculations. The positions of each atom were optimized without SOC in all-up spin configurations until the atomic forces on each atom were $< 1.0 \text{ meV/\AA}$. The K -points were sampled on a $7 \times 7 \times 7 \Gamma$ -centered mesh in the Brillouin zone.

III. RESULTS

A. Density functional results

DFT results showed that the local magnetic spin moment on each Mn is $4.27\mu_B$ in a collinear spin configuration, where

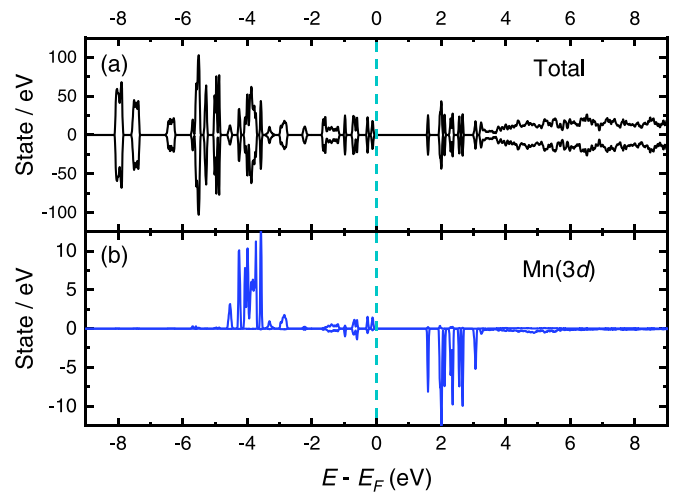


FIG. 2. Without spin-orbit coupling: (a) the total density of states of $\text{Mn}_4\text{Te}_4(\text{PEt}_3)_4$ in the two-up-two-down spin configuration. (b) The projected density of states (PDOS) for Mn(3d) orbitals. Positive and negative values refer to spin-majority and spin-minority channels, respectively. The Fermi energy is set to zero.

two of four Mn spins are up and other two are down, without SOC. As shown in Fig. 2(a), the total density of states (DOS) has a gap ~ 1.5 eV, indicating an insulating nature. The corresponding projected DOS (PDOS) results [see Fig. 2(b)] show that all Mn(3d) components in the spin-majority channel are fully occupied, while almost all Mn(3d) components in the spin-minority are above the Fermi energy. Thus, each Mn ion has five spin-up electrons half filling the d orbitals, following Hund's rule, and in $\text{Mn}_4\text{Te}_4(\text{PEt}_3)_4$, each Mn displays a $+2$ valence state and $S = \frac{5}{2}$ high spin state.

Because of the absence of inversion symmetry, the exchange interaction between two local magnetic spins on Mn includes an off-diagonal contribution, the DM interaction [12,13]. Because the SOC energy of Te is about one order of magnitude larger than that of Mn, the strength of the DM interaction is not negligible and is highly influenced by the SOC of the two Te atoms linking two neighbor Mn atoms. The direction of the DM interaction driven by each Mn-Te-Mn superexchange path is perpendicular to the Mn-Te-Mn plane according to Moriya's rule [13]. The net direction of the two paths is therefore perpendicular to the Mn-Mn connection and parallel to the Te-Te connection [see Fig. 1(b)]. The spin-spin Hamiltonian that properly includes this interaction for the four $S = \frac{5}{2}$ spins on Mn^{2+} ions with tetrahedral symmetry is given by

$$\mathcal{H}_0 = \sum_{(i,j)} [J \mathbf{S}_i \cdot \mathbf{S}_j + \mathbf{D}_{ij} \cdot (\mathbf{S}_i \times \mathbf{S}_j)] - K_u \sum_i (\mathbf{M}_i \cdot \mathbf{S}_i)^2, \quad (1)$$

where J is the Heisenberg interaction and $\mathbf{D}_{ij} = D \hat{\mathbf{D}}_{ij}$ is the DM vector with the direction $\hat{\mathbf{D}}_{ij}$ for two local spins on neighboring Mn sites i and j [see Fig. 1(c)]. Here, K_u is the magnitude of the magnetic anisotropy (note that K_u is often denoted as D in the molecular magnet literature), and \mathbf{M}_i is a unit vector which represents the direction of the magnetic anisotropy on Mn site i . Because of the tetrahedral

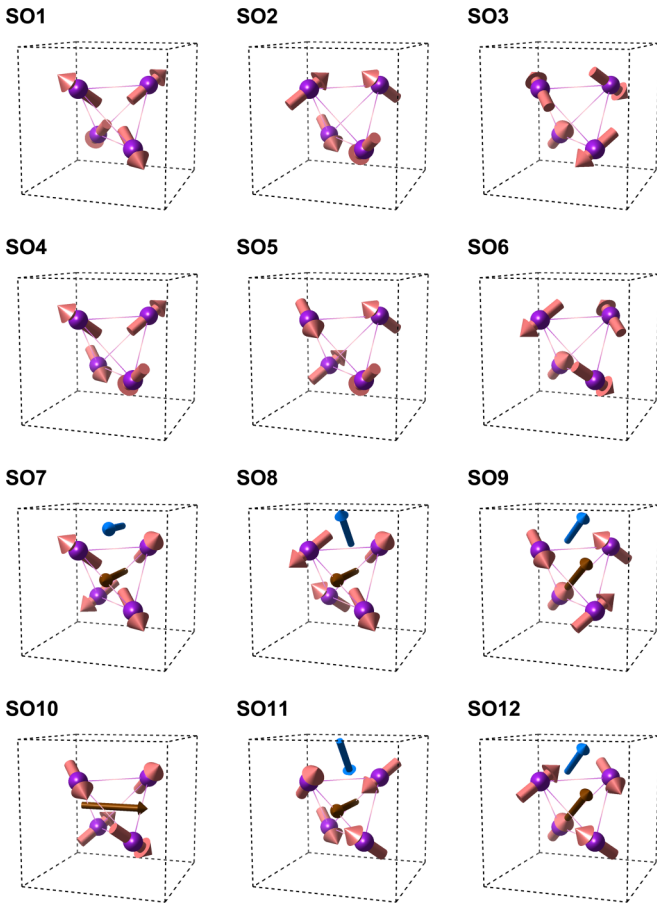


FIG. 3. Twelve noncollinear spin configurations, labeled SO1–SO12, used for total energy calculations and electric dipole calculations. Brown and blue arrows correspond to the directions of the total magnetization and the electric dipole moment for each spin configuration, respectively.

symmetry, \mathbf{M}_i is directed from Mn site i to the body center of the tetrahedron [see Fig. 1(d)].

Based on the Hamiltonian, we investigate the magnetic properties of $\text{Mn}_4\text{Te}_4(\text{PEt}_3)_4$ by calculating total energies for two collinear spin configurations along the [111] direction of the cubic crystalline lattice, all-up and two-up-two-down, and 12 noncollinear spin configurations, labeled SO1–SO12, including six zero-magnetization configurations and six nonzero-magnetization configurations, shown in Fig. 3. The relative total energies are listed in Table I. We transfer spin configurations into quantum spin states and obtain the parameters (J , D , K_u , etc.) through an overdetermined system of linear equations (see Appendix for details). We obtained two solutions based on two set of configurations: $J = 14.02$ meV, $D = -0.44$ meV, and $K_u = 0.26$ meV, labeled as Sol1, is determined from the equations containing all 14 spin configurations. Also, $J = 14.21$ meV, $D = -0.51$ meV, and $K_u = 0.31$ meV, labeled as Sol2, is determined from the equations containing the 12 noncollinear spin configurations.

The residuals labeled as Res1 and Res2 for the configurations using Sol1 and Sol2, respectively, are shown in Table I. For Sol1, the two collinear configurations dominate the

TABLE I. The relative total energies, the residuals of the solutions (Res1 and Res2 corresponding to Sol1 and Sol2), and the magnitude of the dipole moment for each spin configuration. SO1–SO12 correspond to the noncollinear spin configurations shown in Fig. 3. CO-uudd and CO-uuuu correspond to two collinear configurations along the [111] direction of the cubic crystalline lattice, all-up and two-up-two-down, respectively.

	E (meV)	Res1 (meV)	Res2 (meV)	P ($e\text{\AA}$)
SO1	0.00	2.56	0.78	0.000
SO2	-20.80	3.48	-1.69	0.000
SO3	-17.32	4.98	0.65	0.000
SO4	-24.27	3.54	-1.02	0.000
SO5	-9.17	5.21	1.11	0.000
SO6	-17.3	4.98	0.65	0.000
SO7	275.94	-3.34	-2.62	0.012
SO8	265.13	2.50	2.37	0.019
SO9	208.24	-0.58	-0.95	0.058
SO10	276.83	-0.80	-0.70	0.000
SO11	265.13	2.50	2.37	0.019
SO12	208.24	-0.58	-0.95	0.058
CO-uudd	12.11	-24.46	—	0.000
CO-uuuu	946.43	-118.82	—	0.000

residuals, especially the all-up one. However, the solution works well for the noncollinear configurations which we focus on. The large deviation of the energy for CO-uuuu is due to its highest energy, which is far above others. Its electronic properties such as orbital energies are different from other configurations, and a simple spin model is not enough to describe such behavior. With the two collinear configurations excluded, the Sol2 residuals for the 12 noncollinear spin configurations generally decrease significantly. The mean square of the 12 noncollinear residuals for Sol1 is 3.32 meV, and the dispersion about the average of 2.03 meV (biased by the large contribution of the collinear terms) is 2.61 meV, while the dispersion of the Sol2 residuals (average value zero) is 1.50 meV.

Both solutions provide positive J , negative D , and positive K_u . Positive J indicates antiferromagnetic coupling. Negative D indicates the handedness of the spiral coupling, so that the DM interaction favors the coplaner (SO2 or SO4, etc.) instead of the all-in/all-out (SO1) spin configuration. Positive K_u means that each \mathbf{M}_i of site i is an easy axis. The Sol2 solution is chosen in the following discussions. The electric dipole moments are calculated for each spin configuration. According to the results shown in Table I, both collinear spin configurations and all six noncollinear configurations with zero magnetization have zero dipole moments. Among noncollinear configurations from SO7 to SO12, SO7 has a nonzero electric dipole moment $0.012 e\text{\AA}$ along the [100] direction, the same as the direction of its net magnetization. Spin configurations SO8 and SO11, with the same magnetization along the [100] direction, provide an electric dipole of the same magnitude $0.019 e\text{\AA}$ and opposite orientations along the [101] direction. Both SO9 and SO12 retain a threefold rotation axis along the [111] direction with nonzero magnetization and dipole moment $0.058 e\text{\AA}$ along the same direction. Configuration SO10 has a zero electric dipole moment. All

dipole moments are plotted in Fig. 3. Note that the atomic positions as well as the lattice are fixed, so that the calculated dipole moments are purely from charge density displacement driven by noncollinear spin ordering. The dipole moments are not changed significantly when the atomic positions are relaxed in their spin configurations, so that the results are robust.

The spin-dependent electric dipole moments do not change magnitude or sign when all spins are reversed, indicating that the dipole is a function of even order in spins. SO11 is the spin configuration where spins on Mn1 and Mn2, Mn3 and Mn4 are exchanged from SO8, reversing the direction of the dipole moment. Furthermore, SO9 and SO12, with opposite spin chiralities, result in the same dipole moment, so the dipole moment is not relevant to chiral spin textures. Based on the dipole moment results from DFT and analysis based on symmetry properties, we obtain the spin-dependent electric dipole moment as a function of spins as

$$\mathbf{P} = \alpha \sum_{(i,j)} \hat{\mathbf{e}}_{ij} \times (\mathbf{S}_i \times \mathbf{S}_j), \quad (2)$$

where $\hat{\mathbf{e}}_{ij}$ is the direction from site i to j . The magnitude of the coefficient α is $\sim 0.005\text{--}0.035 e\text{\AA}$ in $\text{Mn}_4\text{Te}_4(\text{PET}_3)_4$ based on different spin configurations with nonzero spin-dependent electric dipole moments. Here, we demonstrate that, even at the single molecular scale, the DM-induced electric dipoles are still valid.

We also investigated the magnetic and dielectric properties under hydraulic external strain by modulating the lattice constant by $\pm 1\%$ in length. The corresponding applied pressure is ~ 1.39 kilobar (0.139 GPa) which is a large value for molecular systems. The atomic positions are relaxed under all-up spin configurations without SOC and the total energies relative to SO1; the dipole moments of SO12 are obtained under SOC. As a result, the changes of Mn-Mn connections are $\pm 0.02 \text{\AA}$, and the changes of Mn-Te-Mn bond angles are $\pm 0.3^\circ$. The changes of dipole moments are $\mp 0.003 e\text{\AA}$ ($\sim \mp 6\%$), and the changes of total energies relative to SO1 are $\mp 6.38 \text{ meV}$ ($\sim \mp 1\%$). All responses show almost the same magnitude and opposite sign under the same magnitude and opposite sign of the applied strain. Therefore, no significant response is identified. This indicates that the magnetic (J , D , K_μ , etc.) and dielectric properties here are insensitive to hydraulic strain.

B. Quantum spin model

Once the spin-dependent electric dipole moment is determined, the Hamiltonian for the response to external magnetic field and electric field is given by

$$\mathcal{H} = \mathcal{H}_0 - \mathbf{B} \cdot \sum_i \mathbf{S}_i - \mathbf{E} \cdot \mathbf{P}, \quad (3)$$

where \mathbf{E} is the electric field, \mathbf{P} is the spin-driven polarization, and $\mathbf{B} = g\mu_B\mu_0\mathbf{H}$ is proportional to the magnetic field \mathbf{H} . The electric field is coupled with spins since the electric dipole moment is a function of spin as in Eq. (2), with $\alpha = 0.035 e\text{\AA}$

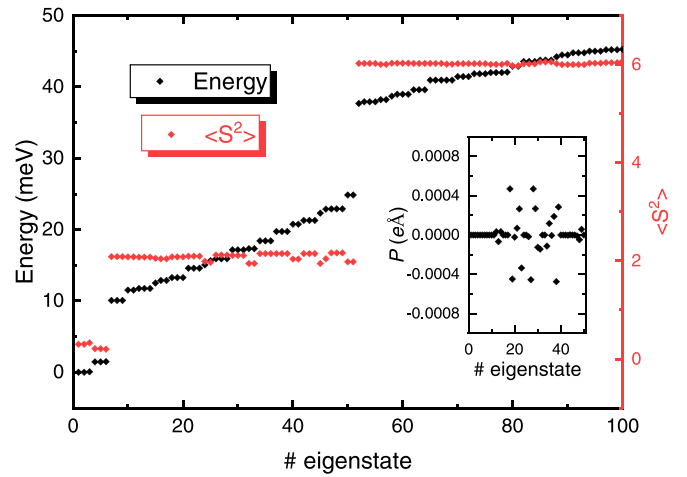


FIG. 4. Without external magnetic and electric fields, the eigenvalues (energies) and the expectation value of $\langle S^2 \rangle$ of the first 100 eigenstates. The energy of the ground state is set to zero. Insert: The expectation value of the dipole moment for the first 51 eigenstates.

chosen. We diagonalized the Hamiltonian matrix for various \mathbf{B} and \mathbf{E} and obtained the total $6^4 = 1296$ eigenvalues and eigenstates. The corresponding quantum spin states and the expectation values of polarization are also obtained.

The eigenvalues and the expectation value of $\langle S^2 \rangle$ of the first 100 eigenstates under zero magnetic and electric field are shown in Fig. 4. Note that, because of the DM interaction in the Hamiltonian, the total spin S of the molecule is not a good quantum number, and the expectation value of $\langle S^2 \rangle$ is not precisely $S(S+1)$ for each eigenstate. However, since $D \ll J$ in $\text{Mn}_4\text{Te}_4(\text{PET}_3)_4$, the integer spin quantum number can still be used to label the spin states. The first six eigenstates with the lowest energies ($\langle S^2 \rangle$ close to zero, so that these states correspond to a $S = 0$ quantum spin state. The next 45 states, which are ~ 10 meV higher than the $S = 0$ states, have $\langle S^2 \rangle$ near 2, corresponding to a $S = 1$ state. The final 49 eigenstates are ~ 40 meV higher than $S = 0$ states and have $\langle S^2 \rangle$ near 6, corresponding to a $S = 2$ state. Considering that the energy scale of external fields is several millielectronvolts, we focus on $S = 0$ and 1 states.

The results of expectation values of polarization for $S = 0$ and 1 states are shown in the insert of Fig. 4. All six of the $S = 0$ states have zero dipole moments. Some $S = 1$ states have a nonzero polarization, but the magnitude of the dipole moment is much smaller than the nonzero dipole obtained from DFT calculations. It is because, according to the DFT results, the spin configurations with nonzero dipole such as SO9 and SO12 have nonzero total magnetization and are > 200 meV higher in energy than the spin configurations with zero magnetization. Therefore, the quantum spin states $S = 1$, the superposition of classical spin configurations, are dominated by zero magnetization configurations and only have very small nonzero dipole moments.

Based on the eigenvalues, eigenstates, and the corresponding expectation values of spins and dipoles of the quantum spin model, we obtained thermal properties of that system. The corresponding partition function Z , thermal average of

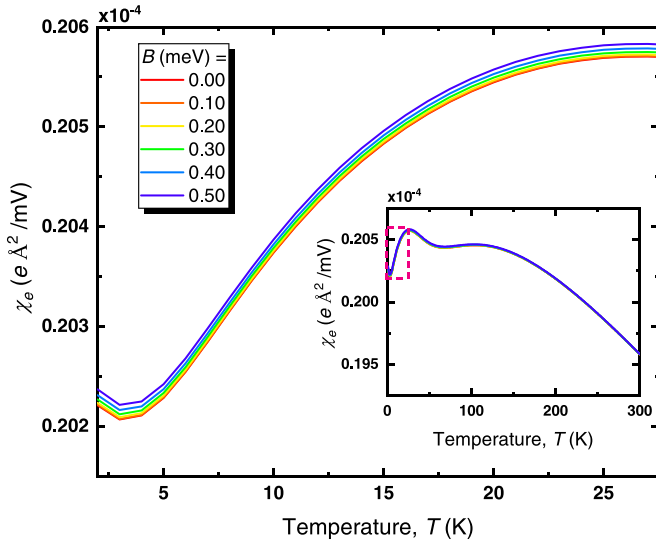


FIG. 5. The electric susceptibility as a function of temperature with various magnetic fields. The red dashed rectangle in the insert panel shows the region expanded in the main panel. The direction of electric susceptibility is perpendicular to the direction of the magnetic field [along the c axis in Fig. 1(a)].

magnetization $\bar{\mathbf{m}}$, and dipole $\bar{\mathbf{P}}$ at finite temperature $\beta = 1/k_B T$ are given by

$$Z(\mathbf{E}, \mathbf{B}, \beta) = \sum_i \exp(-\beta \varepsilon_i), \quad (4)$$

$$\bar{\mathbf{m}}(\mathbf{E}, \mathbf{B}, \beta) = \frac{g\mu_B}{Z} \sum_i \langle \mathbf{S} \rangle \exp(-\beta \varepsilon_i), \quad (5)$$

$$\bar{\mathbf{P}}(\mathbf{E}, \mathbf{B}, \beta) = \frac{1}{Z} \sum_i \langle \mathbf{P} \rangle \exp(-\beta \varepsilon_i), \quad (6)$$

where the summation is over all eigenvalues $\{\varepsilon_i\}$. Then the corresponding electric susceptibility χ_e which depends on magnetic fields is given by

$$\chi_e(\mathbf{E}, \mathbf{B}, \beta) = \frac{\partial \bar{\mathbf{P}}(\mathbf{B}, \mathbf{E})}{\partial \mathbf{E}}. \quad (7)$$

Similarly, the magnetic susceptibility χ_m influenced by electric fields is given by

$$\chi_m(\mathbf{E}, \mathbf{B}, \beta) = \frac{\partial \bar{\mathbf{m}}(\mathbf{B}, \mathbf{E})}{\partial \mathbf{B}}. \quad (8)$$

The temperature-dependent results for χ_e and χ_m are shown in Figs. 5 and 6, respectively. In the inserts for both χ_e and χ_m , dashed contours identify the region of nonzero ME response, where χ_e can be affected by magnetic fields, and χ_m is modulated by the electric fields, though the magnitude of the ME coupling is very small.

All the electric susceptibility curves have a local minimum at $T \sim 3$ K and a local maximum at $T \sim 25$ K. Meanwhile, all the magnetic susceptibility curves have a local maximum at about $T \sim 3$ K and a local minimum at $T \sim 25$ K. Since the energy of ~ 2.2 meV corresponding to 25 K is much smaller than the energy gap between $S = 0$ and 1 states, the thermal average of χ_e and $\chi_m < 25$ K is determined by only the first six $S = 0$ states. For each eigenstate i , the contribution to

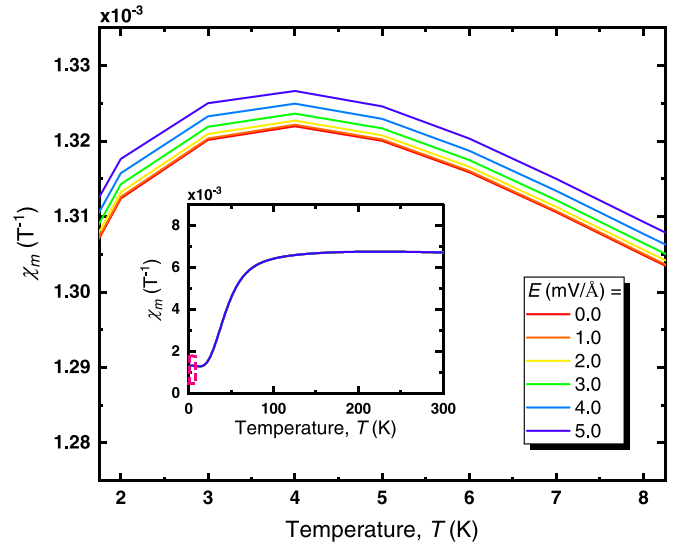


FIG. 6. The magnetic susceptibility as a function of temperature with various electric fields. The red dashed rectangle in the insert panel shows the region expanded in the main panel. The direction of magnetic susceptibility is perpendicular to the direction of the electric fields [along the b axis in Fig. 1(a)].

χ_m is proportional to the fluctuation of spins $\langle \mathbf{S}^2 \rangle - \langle \mathbf{S} \rangle^2$, and $\langle \mathbf{S} \rangle = 0$ when $B = 0$, so that $\chi_m^{(i)} \propto \langle \mathbf{S}^2 \rangle$. Therefore, at finite temperature, $\chi_m \propto \sum_i \langle \mathbf{S}^2 \rangle \exp(-\beta \varepsilon_i)$. The $\langle \mathbf{S}^2 \rangle$ values of the first six eigenstates are 0.251, 0.251, 0.269, 0.166, 0.166, and 0.158 from low to high eigenvalues, respectively. The third eigenstate, with the highest $\langle \mathbf{S}^2 \rangle$ among the six $S = 0$ states, is only 0.09 meV (1.04 K) higher than the doubly degenerate ground states. This leads to the small peak of χ_m at $T \sim 3$ K. On the other hand, the three higher eigenstates with a gap ~ 1.18 meV (13.7 K) above the ground states have lower $\langle \mathbf{S}^2 \rangle$ than the three lower eigenstates. This leads to the small valley in χ_m at $T \sim 25$ K. Then above $T \sim 50$ K, a rise in χ_m appears as temperature increases. This is because, as temperature increases, more $S = 1$ states contribute to an increase in $\langle \mathbf{S}^2 \rangle$. Note that the antiferromagnetic character is robust for all temperature regions up to 300 K, so that χ_m does not follow the paramagnetic behavior $\chi_m \propto 1/T$.

To further investigate the ME coupling, we obtained the change of χ_e as a function of B and the change of χ_m as a function of E , shown in Fig. 7. The fitted dotted lines show a robust quadratic relation, so that $\chi_e \sim B^2$ and $\chi_m \sim E^2$. Since the ME coupling originates from the dipole moment term, which involves the cross-product of two spins, the quadratic relation is the leading order, with the zero linear term according to linear response theory. Further, the quadratic relations mean that the inversion of magnetic/electric fields leaves invariant χ_e/χ_m . It is also consistent with the DFT result that flipping spins leaves the total dipole moment invariant.

The magnitude of the ME coupling from the quantum spin model is much smaller than that found from the DFT calculations. The reason is the quantum spin in a finite system. In contrast to frustrated systems in solids where magnetic spins are regarded as classical spin vectors, spins of frustrated systems in molecular magnets often exhibit their quantum nature. In solids, spin vectors can rotate continuously with

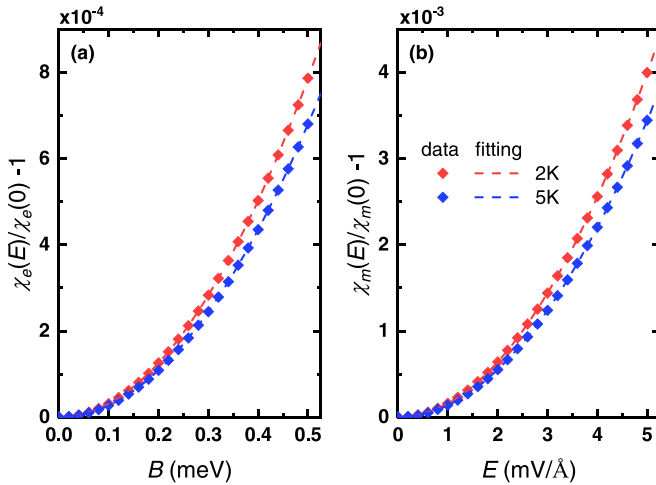


FIG. 7. At 2 and 5 K, (a) the change of electric susceptibility as a function of magnetic field B and (b) the change of magnetic susceptibility as a function of electric field E . Solid diamonds are the data, and dashed lines are the results of quadratic fitting.

external fields since the system is gapless. In a quantum spin system, there is a gap between different quantum spin states, and the magnitude of the gap is positively correlated with the magnitude of the exchange interaction, DM interaction, and magnetic anisotropy. Once the energy of the external field is much smaller than the gap, the response is limited.

C. Implication for experimental measurements

Figure 7(b) shows the predicted change in spin susceptibility for experimentally accessible E fields. The fractional change in magnetic susceptibility at 2 K for $E = 0.10 \text{ V/\AA}$ (or 1 MV/m) is

$$\frac{\Delta\chi_m(E)}{\chi_m(0)} \approx 3 \times 10^{-6}. \quad (9)$$

Although the change is very small, it is within the range of modern high sensitivity techniques for measuring radiofrequency susceptibility [34]. For typical experimental applied field strengths of order of $3 \times 10^5 \text{ V m}^{-1}$, the fractional change in the magnetic susceptibility is $\Delta\chi_m(E)/\chi_m(0) \approx 2 \times 10^{-7}$ which is comparable with experimental capabilities of the order of 1×10^{-7} in the relevant temperature range.

It is also significant that the dependence of the change in magnetic susceptibility on electric field strength is quadratic, as shown in Fig. 7. The absence of a linear electric effect is due to the lack of large strain dependence. The ME effect is caused by a superexchange interaction via Mn-Te-Mn or symmetric striction. Because of the quadratic dependence on field strength, experiments should be designed for the highest possible values of E within limitations imposed by electrical breakdowns of sample cell materials and thermal bonding agents used for the samples.

One should note that the coefficient α in Eq. (2) is a spin-dependent scalar in terms of the studies of Katsusa *et al.* [14,15]. The current treatment of a constant α is just a

simplified estimation. Furthermore, αE is the independent variable in the numerical simulations. It means that, to approach the same response, one requires a smaller electric field with the larger α and vice versa. Electric field E has a linear relation and a quadratic relation with χ_e and χ_m , respectively, so that it is straightforward to obtain that, with $\alpha = 0.005 e\text{\AA}$, the lower limit we obtained, the responses of $\chi_e - B$ and $\chi_m - E$ are $\frac{1}{7}$ and $\frac{1}{49}$ of that with $\alpha = 0.035 e\text{\AA}$, respectively.

IV. CONCLUSIONS

In summary, we first investigated the magnetic properties of the crystalline phase of $\text{Mn}_4\text{Te}_4(\text{PEt}_3)_4$ based on first-principles calculations. Each Mn has a $S = \frac{5}{2}$ high spin state. The antiferromagnetic coupling leading to frustrated spins and the noncollinear DM interaction as well as the magnetic anisotropy was identified and quantized. A nonzero electric dipole moment was obtained in noncollinear spin configurations based on Berry phase calculations. The magnitude of the dipole moment follows the formula $\sim \hat{\mathbf{e}}_{ij} \times (\mathbf{S}_i \times \mathbf{S}_j)$, so that the electric dipole is coupled with a noncollinear magnetic moment, and we thus found the DM-induced ME effect in the single molecular scale. After parameterizing the spin-spin Hamiltonian, we studied the quantum spin model based on the eigenvalues and eigenstates found by the direct diagonalization of the Hamiltonian. The magnetic susceptibility χ_m is changed by the electric field E , and the electric susceptibility χ_e is changed by the magnetic field B , though the change is small. Further studies showed quadratic relations between both χ_m and E , and χ_e and B , respectively. Such a ME effect is expected to be observable in experiments.

ACKNOWLEDGMENTS

This paper is supported as part of the Center for Molecular Magnetic Quantum Materials, an Energy Frontier Research Center funded by the U.S. Department of Energy, Office of Science, Basic Energy Sciences under Award No. DE-SC0019330. Computations were performed at the National Energy Research Scientific Computing Center and the University of Florida Research Computing (UFRC) Center.

APPENDIX: PARAMETERS OBTAINED FROM TOTAL ENERGY BASED ON DFT FOR A QUANTUM SPIN HAMILTONIAN

For a spin configuration α , each local magnetic spin i on a magnetic atom has a normalized classical spin vector $\mathbf{e}_i = (e_{ix}, e_{iy}, e_{iz})$ and spin quantum number s_i . Diagonalizing the spin matrix $\mathbf{e}_i \cdot \mathbf{S}_i$, where \mathbf{S}_i is the matrix of the spin operator in terms of s_i , we obtain the quantum spin state for this spin in the basis of $|s_{iz}\rangle$ and the eigenvector $|\alpha_i\rangle$ with the eigenvalue $+s_i$. The quantum spin state containing n spins for this spin configuration is $|\alpha\rangle = |\alpha_1\rangle \otimes |\alpha_2\rangle \otimes \cdots \otimes |\alpha_n\rangle$, where \otimes is the outer product. The total energy based on spin configuration α is

$$E_\alpha = E_0 + \langle \alpha | \mathcal{H}_0 | \alpha \rangle, \quad (\text{A1})$$

where

$$\begin{aligned} \langle \alpha | \mathcal{H}_0 | \alpha \rangle &= J \sum_{\langle i,j \rangle} \langle \alpha | \mathbf{S}_i \cdot \mathbf{S}_j | \alpha \rangle \\ &+ D \sum_{\langle i,j \rangle} \langle \alpha | \hat{\mathbf{D}}_{ij} \cdot (\mathbf{S}_i \times \mathbf{S}_j) | \alpha \rangle \\ &- K_u \sum_i \langle \alpha | (\mathbf{M}_i \cdot \mathbf{S}_i)^2 | \alpha \rangle, \end{aligned} \quad (\text{A2})$$

and E_0 is the spin-irrelevant energy. According to a suggestion by Ruiz *et al.* [35,36], when the spin-broken symmetric antiferromagnetic spin ordering includes overlapped occupied molecular orbitals, a correction of $1 + \min(S_i, S_j)/2S_iS_j$ is included for obtaining the expectation values of the exchange interaction terms.

We obtain the (linear) parameters J , D , and K_s by a least squares minimization of the sum of differences between E_{α_i}

and the total energy (the relative total energy) of that configuration obtained from DFT calculations. Assume there are N such configurations so that $\alpha = \alpha_1, \alpha_2, \dots, \alpha_N$. By writing $E_0 = E_{\text{DFT}_0} + \delta$, where E_{DFT_0} is the lowest energy from DFT calculations (note that δ is a small quantity), we have N spin configurations which give rise to N differences:

$$\begin{aligned} E_{\alpha_1} - E_{\text{DFT}_0} &= \langle \alpha_1 | \mathcal{H}_0 | \alpha_1 \rangle + \delta, \\ E_{\alpha_2} - E_{\text{DFT}_0} &= \langle \alpha_2 | \mathcal{H}_0 | \alpha_2 \rangle + \delta, \\ &\dots \\ E_{\alpha_N} - E_{\text{DFT}_0} &= \langle \alpha_N | \mathcal{H}_0 | \alpha_N \rangle + \delta. \end{aligned} \quad (\text{A3})$$

The number of configurations N is chosen to be larger than the number of parameters (E_0 , J , D , K_u , and δ) to be determined, an overdetermined system. Then the parameters J , D , and K_u are the least squares minimization of Eq. (A3). The residuals for each spin configuration are also obtained based on the solution.

-
- [1] S.-W. Cheong and M. Mostovoy, Multiferroics: A magnetic twist for ferroelectricity, *Nat. Mater.* **6**, 13 (2007).
- [2] N. A. Spaldin, S.-W. Cheong, and R. Ramesh, Multiferroics: Past, present, and future, *Phys. Today* **63**(10), 38 (2010).
- [3] S. Fusil, V. Garcia, A. Barthélemy, and M. Bibes, Magneto-electric devices for spintronics, *Annu. Rev. Mater. Res.* **44**, 91 (2014).
- [4] M. Fiebig, T. Lottermoser, D. Meier, and M. Trassin, The evolution of multiferroics, *Nat. Rev. Mater.* **1**, 16046 (2016).
- [5] J.-P. Rivera, A short review of the magnetoelectric effect and related experimental techniques on single phase (multi-) ferroics, *Eur. Phys. J. B* **71**, 299 (2009).
- [6] H. Schmid, Magnetoelectric effects in insulating magnetic materials, *Proc. SPIE* **4097**, 12 (2000).
- [7] S. Chikara, J. Gu, X.-G. Zhang, H.-P. Cheng, N. Smythe, J. Singleton, B. Scott, E. Krenkel, J. Eckert, and V. S. Zapf, Magneto-electric behavior via a spin state transition, *Nat. Commun.* **10**, 4043 (2019).
- [8] J.-X. Yu, D.-T. Chen, J. Gu, J. Chen, J. Jiang, L. Zhang, Y. Yu, X.-G. Zhang, V. S. Zapf, and H.-P. Cheng, Three Jahn-Teller States of Matter in Spin-Crossover System Mn(taa), *Phys. Rev. Lett.* **124**, 227201 (2020).
- [9] V. S. Zapf, P. Sengupta, C. D. Batista, F. Nasreen, F. Wolff-Fabris, and A. Paduan-Filho, Magnetoelectric effects in an organometallic quantum magnet, *Phys. Rev. B* **83**, 140405(R) (2011).
- [10] M. Yazback, J.-X. Yu, S. Liu, L. Zhang, N. S. Sullivan, and H.-P. Cheng, First-principles study of an $S = 1$ quasi one-dimensional quantum molecular magnetic material, *Phys. Rev. B* **103**, 054434 (2021).
- [11] V. B. Jakobsen, S. Chikara, J.-X. Yu, E. Dobbelaar, C. T. Kelly, X. Ding, F. Weickert, E. Trzop, E. Collet, H.-P. Cheng, G. G. Morgan, and V. S. Zapf, Giant magnetoelectric coupling and magnetic-field-induced permanent switching in a spin crossover Mn(III) complex, *Inorg. Chem.* **60**, 6167 (2021).
- [12] I. Dzyaloshinsky, A thermodynamic theory of “weak” ferromagnetism of antiferromagnetics, *J. Phys. Chem. Solids* **4**, 241 (1958).
- [13] T. Moriya, Anisotropic superexchange interaction and weak ferromagnetism, *Phys. Rev.* **120**, 91 (1960).
- [14] H. Katsura, N. Nagaosa, and A. V. Balatsky, Spin Current and Magnetoelectric Effect in Noncollinear Magnets, *Phys. Rev. Lett.* **95**, 057205 (2005).
- [15] H. Katsura, A. V. Balatsky, and N. Nagaosa, Dynamical Magnetoelectric Coupling in Helical Magnets, *Phys. Rev. Lett.* **98**, 027203 (2007).
- [16] T. Kimura, Spiral magnets as magnetoelectrics, *Annu. Rev. Mater. Res.* **37**, 387 (2007).
- [17] A. K. Boudalis, J. Robert, and P. Turek, First demonstration of magnetoelectric coupling in a polynuclear molecular nanomagnet: single-crystal EPR studies of $[\text{Fe}_3\text{O}(\text{O}_2\text{CPh})_6(\text{py})_3]\text{ClO}_4 \cdot \text{py}$ under static electric fields, *Chem. Eur. J.* **24**, 14896 (2018).
- [18] J. Robert, N. Parizel, P. Turek, and A. K. Boudalis, Polyanisotropic magnetoelectric coupling in an electrically controlled molecular spin qubit, *J. Am. Chem. Soc.* **141**, 19765 (2019).
- [19] J. H. Yang, Z. L. Li, X. Z. Lu, M.-H. Whangbo, S.-H. Wei, X. G. Gong, and H. J. Xiang, Strong Dzyaloshinskii-Moriya Interaction and Origin of Ferroelectricity in Cu_2OSeO_3 , *Phys. Rev. Lett.* **109**, 107203 (2012).
- [20] S. Seki, S. Ishiwata, and Y. Tokura, Magnetoelectric nature of skyrmions in a chiral magnetic insulator Cu_2OSeO_3 , *Phys. Rev. B* **86**, 060403(R) (2012).
- [21] S. Seki, X. Z. Yu, S. Ishiwata, and Y. Tokura, Observation of skyrmions in a multiferroic material, *Science* **336**, 198 (2012).
- [22] J. S. White, K. Prša, P. Huang, A. A. Omrani, I. Živković, M. Bartkowiak, H. Berger, A. Magrez, J. L. Gavilano, G. Nagy *et al.*, Electric-Field-Induced Skyrmion Distortion and Giant Lattice Rotation in the Magnetoelectric Insulator Cu_2OSeO_3 , *Phys. Rev. Lett.* **113**, 107203 (2014).
- [23] E. Ruff, P. Lunkenheimer, A. Loidl, H. Berger, and S. Krohns, Magnetoelectric effects in the skyrmion host material Cu_2OSeO_3 , *Sci. Rep.* **5**, 15025 (2015).
- [24] P. E. Blöchl, Projector augmented-wave method, *Phys. Rev. B* **50**, 17953 (1994).

- [25] G. Kresse and D. Joubert, From ultrasoft pseudopotentials to the projector augmented-wave method, *Phys. Rev. B* **59**, 1758 (1999).
- [26] G. Kresse and J. Furthmüller, Efficiency of *ab-initio* total energy calculations for metals and semiconductors using a plane-wave basis set, *Comput. Mater. Sci.* **6**, 15 (1996).
- [27] G. Kresse and J. Furthmüller, Efficient iterative schemes for *ab initio* total-energy calculations using a plane-wave basis set, *Phys. Rev. B* **54**, 11169 (1996).
- [28] J. P. Perdew, K. Burke, and M. Ernzerhof, Generalized Gradient Approximation Made Simple, *Phys. Rev. Lett.* **77**, 3865 (1996).
- [29] V. I. Anisimov, I. V. Solovyev, M. A. Korotin, M. T. Czyżyk, and G. A. Sawatzky, Density-functional theory and NiO photoemission spectra, *Phys. Rev. B* **48**, 16929 (1993).
- [30] S. Grimme, J. Antony, S. Ehrlich, and H. Krieg, A consistent and accurate *ab initio* parametrization of density functional dispersion correction (DFT-D) for the 94 elements H-Pu, *J. Chem. Phys.* **132**, 154104 (2010).
- [31] R. D. King-Smith and D. Vanderbilt, Theory of polarization of crystalline solids, *Phys. Rev. B* **47**, 1651 (1993).
- [32] R. Resta, Macroscopic polarization in crystalline dielectrics: the geometric phase approach, *Rev. Mod. Phys.* **66**, 899 (1994).
- [33] B. Choi, D. W. Paley, T. Siegrist, M. L. Steigerwald, and X. Roy, Ligand control of manganese telluride molecular cluster core nuclearity, *Inorg. Chem.* **54**, 8348 (2015).
- [34] A. Sirusi, J. Adams, M. Lewkowitz, R. Sun, and N. S. Sullivan, A tunnel diode oscillator for high sensitivity broad temperature range susceptibility measurements, [arXiv:2109.11030](https://arxiv.org/abs/2109.11030).
- [35] E. Ruiz, J. Cano, S. Alvarez, and P. Alemany, Broken symmetry approach to calculation of exchange coupling constants for homobinuclear and heterobinuclear transition metal complexes, *J. Comput. Chem.* **20**, 1391 (1999).
- [36] E. Ruiz, A. Rodríguez-Fortea, J. Cano, S. Alvarez, and P. Alemany, About the calculation of exchange coupling constants in polynuclear transition metal complexes, *J. Comput. Chem.* **24**, 982 (2003).